# Experiments and Lagrangian simulations on the formation of droplets in continuous mode

J. R. Castrejón-Pita,[1] N. F. Morrison,[2] O. G. Harlen,[2] G. D. Martin,[1] and I. M. Hutchings[1]
[1]*Institute for Manufacturing, University of Cambridge, Cambridge CB3 0FS, United Kingdom*
[2]*Department of Applied Mathematics, University of Leeds, Leeds LS2 9JT, United Kingdom*
(Received 18 August 2010; revised manuscript received 23 November 2010; published 4 January 2011)

Experimental and computational studies on the dynamics of millimeter-scale cylindrical liquid jets are presented. The influences of the modulation amplitude and the nozzle geometry on jet behavior have been considered. Laser Doppler anemometry (LDA) was used in order to extract the velocity field of a jet along its length, and to determine the velocity modulation amplitude. Jet shapes and breakup dynamics were observed via shadowgraph imaging. Aqueous solutions of glycerol were used for these experiments. Results were compared with Lagrangian finite-element simulations with good quantitative agreement.

DOI: 10.1103/PhysRevE.83.016301 PACS number(s): 47.55.db, 47.80.Jk

## I. INTRODUCTION

The first attempts to formally understand the dynamics of the breakup of continuous liquid jets were made by Savart and Rayleigh in the nineteenth century [1,2]. Subsequently, many groups have continued to develop theoretical models and to conduct experimental investigations to study the process of breakup of liquids and the creation of droplets. Currently, studies of jet breakup have regained importance due to the relevance of drop formation mechanisms to industrial and commercial applications of the noncontact deposition of liquids (i.e., inkjet printing) [3].

Although many studies have contributed to the understanding of droplet creation and evolution, unsolved problems still remain, most of them surrounding the breakup regime which is widely used in the production of droplets for inkjet applications [4,5]. In particular, theoretical and numerical descriptions of the breakup of jets and other flows with an exposed surface present a major challenge due to the so-called "pinch-off" singularity in free-surface flows [4]. The difficulty arises as the Navier-Stokes equation exhibits a singularity as the jet diameter vanishes asymptotically at the pinchoff point [6]. Several analytical and numerical approaches describing free-surface flows have been followed in recent years; a comprehensive review of these studies can be found in [4].

There are two principal methods used to generate droplets in the printing context: drop-on-demand (DOD) and continuous inkjet (CIJ) printing [5,7]. These techniques differ in the way in which the droplets are produced, and tend to be used for different purposes. Generally, DOD printers are used in a range of office and domestic applications, often with multiple colors, while CIJ printing is currently used mainly for date coding and labeling on industrial production lines. This paper focuses on the formation of droplets from a continuous jet, as in the continuous inkjet process; a detailed description of drop formation mechanisms in DOD can be found elsewhere, viz. [7,8]. Continuous jets create drops at higher frequencies than equivalently sized drop-on-demand systems, so they are ideally suited to high speed printing applications. Inkjet printing processes based on continuous inkjet technology continue to be developed and are now used in applications which were, until recently, the preserve of conventional printers [9]. Pushing the boundaries of resolution, speed, and materials requires improved understanding and more accurate simulation of jet breakup and drop and satellite behavior. Numerical simulations offer an attractive tool to explore the complex interacting effects of ink fluid properties, nozzle design, and actuation mechanisms. However, for this to happen, numerical codes require experimental validation.

The study of droplets formed by the breakup of jets is a topic of considerable industrial interest because continuous inkjet printers demand close control of droplet sizes and speeds. In the most common type of CIJ printer, the natural breakup of a continuous jet into a train of droplets is enhanced by the introduction of an oscillating pressure modulation; the velocity and the separation distance of the droplets are determined by the modulation frequency and the size of the nozzle [10,11]. Current models of CIJ aim to predict the jet breakup length and ultimately the physical characteristics of the droplets and their satellites. The overall purpose of most studies is to increase the resolution, versatility, and quality of the printing process. Other studies seek to adapt existing printing techniques to new applications in fields such as electronics and biotechnology. Fundamentally, all of these studies aim to obtain a better understanding of the governing laws behind the formation, evolution, and breakup of continuous jets into droplets.

Experimental studies of jet breakup can be classified into three categories: experiments carried out with commercially available micrometer-scale jet actuators [12,13], millimeter-scale experiments with appropriately chosen fluid parameters designed to replicate the dimensionless quantities of their commercial counterparts [14,15], and fluid dynamical experiments with rather different operating parameters to those used in commercial printers [16,17]. Generally, experiments performed in the first category are complicated and cannot involve direct measurement of many of the parameters involved in the jetting. In most cases, the physical dimensions of commercial droplet actuators and the speed and size of their jets produce conditions where it is impossible to use pressure transducers, thermocouples, and velocimetry techniques such as laser Doppler anemometry (LDA) or particle image velocimetry (PIV) [8]. Consequently, these experiments are restricted to analyzing only externally observable quantities such as droplet size and speed and breakup lengths [3,13,18,19]. In contrast, millimeter-scale systems allow the direct measurement of the flow, pressure, and even velocity profiles [14,15], but may be unable to fully replicate the dimensionless parameters of their commercial counterparts (e.g., gravity is relatively

 

more important over the longer time scales involved in the millimeter-sized system). Finally, experiments performed in the last category may provide conditions conducive to further understanding the variables involved in the behavior of jets and their breakup; these studies are also of industrial importance as they may be used to explore potential new jetting regimes.

Numerical simulations of jet breakup are often performed with the aim of improving the stability of a computational method, or to test its computational stability and/or efficiency, rather than making a direct comparison and validation with experimental results [9,20]. In other numerical studies, the validation with experimental results is limited to contrasting jet shapes qualitatively, and is usually not extended to the comparison of more fundamental variables such as the inner jet dynamics [21,22]. This is partially justified as many experimental studies deal only with variables of industrial interest (such as driving voltages and jet shapes) and not with intrinsic variables (such as pressure or fluid velocity) which complicates the comparison with theoretical and numerical models [12,18]. This work aims to provide a scheme to bridge this theoretical-experimental divide commonly observed in current numerical and experimental studies of the jetting of fluids. It also demonstrates that Lagrangian simulations are appropriate for the study of jets, and thus that this method may be used to study a variety of different scenarios to investigate regions of an experimental setup which are difficult to access experimentally (i.e., positions that cannot be reached by a LDA probe, or to study nontransparent liquids, etc.). A validated numerical code also provides a reliable means of exploring dangerous or hazardous experimental and practical scenarios, such as the jetting of molten metals, aromatic compounds, chemicals or drugs for applications in rapid prototyping, printing electronics, and/or pharmaceuticals.

In this work, a series of experiments and numerical simulations were conducted on millimeter-sized jets under various flow conditions, including those of industrial interest. The experimental setup used in these studies permits the direct measurements of the nozzle properties and their modification. In addition, the fluid used was Newtonian, transparent, and allowed the application of velocimetry and imaging techniques. Laser Doppler anemometry (LDA) and shadowgraph imaging were used in harmonically modulated jets to extract the relationship between the jet breakup length and the amplitude of the velocity modulation amplitude (breakup curves). In unmodulated jets, LDA was used to obtain internal velocity profiles from jets produced by nozzles of the same diameter but with different lengths (aspect ratios). The characteristics of the experimental setup together with the LDA measurements were used to test Lagrangian numerical simulations of a system under similar conditions. Simulations were performed for modulated jets to study the jet breakup behavior and for unmodulated jets to obtain internal velocity profiles. To summarize, the aims of this work are (i) to present a millimeter-sized droplet generator which can reproduce the dynamical conditions found in industrial systems but with the advantage of being fully characterizable and of a simpler operation; (ii) to demonstrate that laser Doppler anemometry can be used in harmonically modulated liquid jets to measure the amplitude of axial velocity oscillations; (iii) to observe the effect of the nozzle geometry on the velocity profile along an unmodulated liquid jet using laser Doppler anemometry; (iv) to present Lagrangian simulations of a system reproducing most of the characteristics of a real droplet generator; and (v) to compare numerical and experimental results of the jetting of Newtonian modulated and unmodulated fluids under different conditions. Experimental and numerical results were found to present good quantitative agreement.

## II. EXPERIMENTAL DETAILS

As previously noted, there are many different actuation mechanisms by which fluid jets may be produced. In most cases, the creation of a droplet is determined by an electric signal that drives a piezoelectric or a heating element inside a printhead to either produce the jetting pressure (DOD) or to enhance the breakup of a continuous jet (CIJ) [5,23]. Although important advances in the understanding of the jetting phenomenon and drop formation have been made in terms of the amplitude and characteristics of this electric signal (often called the wave form) [12,18], few studies have been conducted using a more fundamental driver such as the pressure or velocity wave [15,24].

### A. Jet generation and visualization

The setup used to produce and measure the properties of unmodulated and modulated jets is a modified version of a system that has been described elsewhere [14]. In brief, this droplet generator employs an electrodynamic actuator to produce pressure modulations inside a liquid reservoir; the generator is shown in Fig. 1.

To operate the setup as a continuous jet generator, the inner reservoir was filled with liquid pumped in from an external liquid container, which was also used to receive the jetted liquid; details are shown in Fig. 2. The upper base of the inner liquid reservoir in the jet generator is made of a 2-mm-thick rubber membrane which was used to separate the liquid from the actuator (a LDS Test and Measurement Ltd. V201 vibrator), and to transmit the modulation to the liquid, and finally to the jet. The vibrator oscillates only axially (along the jet axis) in the range from 10 Hz to 10 kHz; the vibrator displacement is not constant within this frequency range [25]. The lower base contains the nozzle plane, and its design permits straightforward replacement of the nozzle by other nozzles of different shapes, as desired. A calibrated

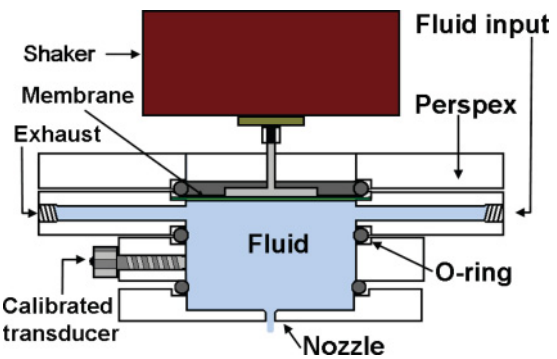


FIG. 1. (Color online) Schematic diagram of the continuous jet droplet generator.

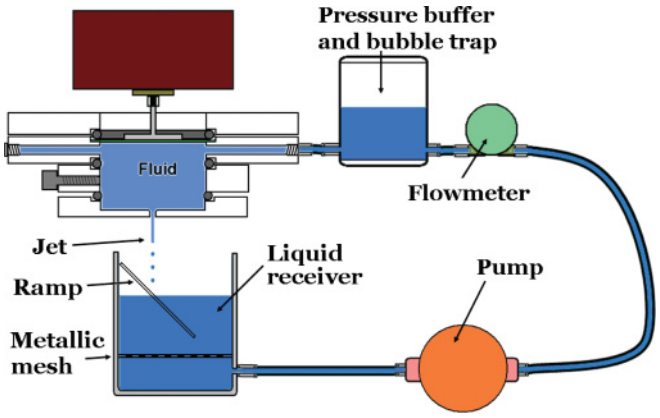


FIG. 2. (Color online) Jet apparatus.

stainless steel diaphragm pressure transducer (Entran Sensors & Electronics, EPX-N12-1B) is positioned in the side of the reservoir with its diaphragm in contact with the liquid. This transducer allows dynamic and static pressure measurements of up to 1 bar, at frequencies of up to 6.5 kHz with linear calibration [26].

To provide stable jetting conditions, the system was purged of air through an exhaust line and the liquid was pumped by a Premotec BL58 pump. Any remaining air was trapped by its buoyancy in the bubble trap (Fig. 2) placed between the pump and the jet generator. A double layer of 0.5-mm stainless steel mesh was placed in the receiver container to prevent air bubbles being pumped back into the lines and the actuator. In addition, the jetted liquid was not allowed to impact directly onto the liquid surface in the receiver; a plastic ramp was used to prevent splashing and hence the production of bubbles. A FHKSC Gigmesa turbine-type flow meter was positioned in the supply lines to monitor and record the flow. The jet speed was controlled by the voltage applied to the pump; speeds of up to $5\,\mathrm{ms}^{-1}$ could be obtained for a system with a 2.2-mm-diameter nozzle and a 74.7% solution of glycerol in water. In order to increase the stability of the jets, cylindrical nozzles with conical inlets were used [27]; the numerical simulations were carried out for the same geometry (see Sec. III B).

For the experiments with modulated jets, the modulation signal applied to the vibrator was produced by a TTi TG550 function generator, amplified by an EAPA 250 audio amplifier (harmonic distortion <0.025% at 1 kHz and 10-W rms). The function generator signal was synchronized to a TTi TGP110 pulse generator to produce transistor-transistor logic (TTL) 5-ms pulses in phase with the modulation signal every half second to activate a relay box consisting of a generic 12-V relay with a 2-ms time response. The relay activated a SB-800 speedlight Nikon flash to illuminate the jet from behind, allowing shadowgraph pictures to be taken. A $30 \times 50$-cm acrylic diffuser was positioned between the jet and the flash to produce an even background for the field of view of a D80 Nikon DSLR camera (10.2-megapixel charge-coupled device with a vibration reduction 18–135-mm lens), which was placed in front of the jet, the diffuser, and the flash. The flash was set to the 1/128-s option to produce light pulses of approximately 24 $\mu$s duration (as measured with a 10530DAL IPL photodiode). Two kinds of illumination were possible with this setup. Strobe illumination was produced by opening the camera shutter for 20 s to allow the recording of 40 flash pulses in a single frame. In contrast, single-flash imaging was also produced with a shutter time of 500 ms which was just long enough to record a single flash event. For the experiments, the camera lens was arranged to produce a field of view of 35 cm in the jet direction and a depth of field of approximately 4 mm; the 600 ISO sensitivity option was used. The resulting optical system had a resolution of 11.5 pixels per mm. Numerous imaging techniques exist to visualize the breakup and creation of droplets. These range from ultrahigh speed imaging for micrometer-sized droplets to single flash photography of millimeter-sized jets [14,28]. For the present experiments, the temporal and spatial resolution achieved by the optical system was appropriate to the scale and speed of the flow (in each frame, a droplet had an average diameter of 44 pixels).

During the experiments the phase between the modulation signal and the strobe light system could be varied by adjusting the delay output of the pulse generator. The phase was adjusted to allow observation and measurement of the precise jet breakup point (i.e., the point on the jet axis where the jet first pinches off). Parallel to the jet, and within the camera's field of view, a reference scale was positioned in order to determine the distance of the breakup point from the nozzle plane (the breakup length). The shadowgraph images were digitally recorded, transferred to a computer, and then individually analyzed.

In the case of unmodulated jets, three nozzle geometries were used for the experiments: their dimensions are illustrated in Fig. 3. These nozzles share a diameter of $d = 2.2$ mm and a 45° conic inlet of 1 mm depth, but differ in their aspect ratios (diameter divided by the length of the cylindrical section of the nozzle): aspect ratios of 0, 1, and 2 were studied. For these experiments, the system was set up to produce an average jet velocity of $3.6\,\mathrm{ms}^{-1}$.

The fluid used in all experiments was a Newtonian mixture of 74.7% glycerol (99.9% pure) with 25.3% tri-distilled water, with a density of $\rho = 1250\,\mathrm{kg\,m}^{-3}$, a surface tension of $\sigma = 0.065\,\mathrm{Nm}^{-1}$ (measured by a bubble pressure tensiometer SITA Messtechnik, Pro line t15, at a bubble lifetime of 100 ms), and

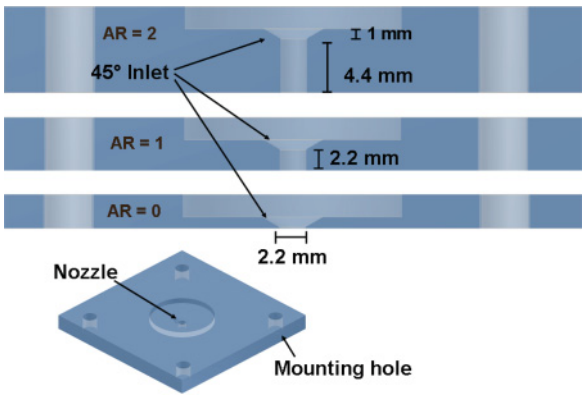


FIG. 3. (Color online) The dimensions of the nozzles of different aspect ratios (AR) machined in perspex for the present work. Dimensions shown in scale.

a viscosity of $\mu = 0.0367$ Pa s (measured by a viscometer Hidramotion, Visco-lite 700); these values were in agreement with those reported in [29]. All of the measurements were taken in a 15°C controlled temperature room. Based on the nozzle radius ($d/2$) and the droplet speed $u$ (measured immediately below the breakup point), the Reynolds and Weber numbers of the jet were defined as

$$\mathrm{Re} = \frac{\rho u d}{2\mu}, \quad \mathrm{We} = \frac{\rho u^2 d}{2\sigma}. \tag{1}$$

### B. Laser Doppler anemometry

Laser Doppler anemometry is a technique that has been used previously in the study of jets to test theoretical models and to study the effects of surfactants on the jet surface [16,17]. However, these studies were not intended to study the effect of nozzle geometry on jet behavior and/or the effects of harmonic modulation on the breakup. In this work, LDA was used to measure the effect of pressure modulation on the internal velocity of a continuous jet and to obtain velocity profiles along the jetting axis of unmodulated jets. The use of a large-scale millimeter-sized nozzle presents many advantages over other commercially available designs, for example, permitting the use of velocimetry and simple imaging techniques such as LDA and shadowgraphy. Traditionally, large-scale models of printheads have been used to study drop formation by shadowgraphy techniques but not by laser anemometry [15]. Laser techniques have been used to determine the breakup point of high speed micrometer jets but in a large-scale system shadowgraph photography provides sufficient spatial resolution to identify the breakup point precisely with a rather simple setup [14,19].

A schematic diagram of the jet-laser geometry in the LDA measurements is shown in Fig. 4. The LDA probe was positioned in such a way that the crossing of the lasers was parallel to the jet axis, and was directed radially inwards toward the center. In this way the measurements were not affected by the optical distortion produced by the liquid interface along the cylindrical region of the jet.

The LDA technique measures the velocity of seeded particles that pass through a measurement volume consisting of a series of equally spaced laser fringes. The fringes are usually created by the intersection of two laser beams. The light scattered by the particles during their journey along the fringes is detected by a photomultiplier and the particle speed $u$ is calculated based on the frequency $f$ of the scattered signal by the equation

$$u = \frac{\lambda_1 f}{2 \sin \theta_1}, \tag{2}$$

where $\lambda_1$ is the wavelength of the laser in the relevant medium and $2\theta_1$ is the angle between the two laser beams; for an extensive review refer to [30]. The use of LDA, especially in media different from air, requires an understanding of how refraction alters the separation, position, and number of the fringes, and the effect of the seeding particles on the flow. The LDA does not require recalibration when used in different optical media, as although the angle between the beams changes (see Fig. 4), the separation of the fringes is

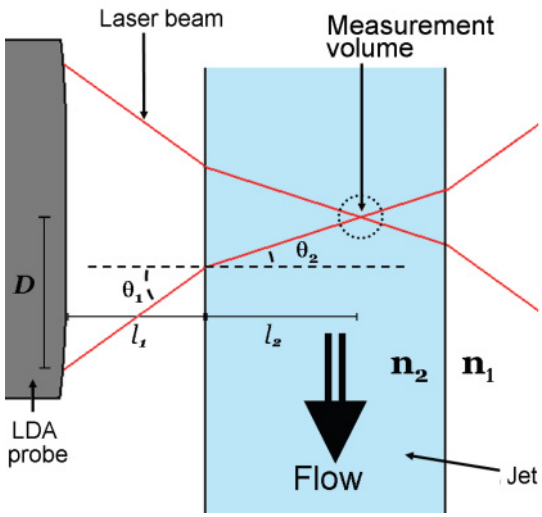


FIG. 4. (Color online) Effects of refraction on the position of the LDA measurement volume within the jet (dimensions not to scale).

kept constant. By Eq. (2), the separation $d_{f_1}$ of the fringes in a particular medium is given by

$$d_{f_1} = \frac{\lambda_1}{2 \sin \theta_1}. \tag{3}$$

When a second medium is introduced, the intersection angle and the wavelength of the lasers change due to refraction. The new angle is calculated by Snell's law and the new wavelength is determined by the ratio of the refractive indices. As a result, the fringe separation $d_{f_2}$ in the second medium is given by

$$d_{f_2} = \frac{\lambda_2}{2 \sin \theta_2} = \frac{n_2}{n_1} \frac{n_1 \lambda_1}{2 n_2 \sin \theta_1} = d_{f_1}, \tag{4}$$

where $n_1$ and $n_2$ are the refractive indices of the first and second media, respectively, and $\lambda_2$ is the laser wavelength in the second medium.

Although the fringe separation does not change inside a second optical medium, the position of the beam intersection does change [17], as illustrated in Fig. 4. To determine the new intersection point, two quantities are defined: $l_1$ as the distance from the front lens of the LDA probe to the interface between the two media, and $l_2$ as the distance from that interface to the intersection point. Applying Snell's law and simple trigonometry, we find

$$l_2 = \frac{D - l_1 \tan \theta_1}{\tan \{\arcsin (n_1 \sin \theta_1 / n_2)\}}, \tag{5}$$

where $2D$ is the original separation of the laser beams in the probe. For the LDA and the liquid used in these experiments, $\lambda_1 = 632.8$ nm, $D = 15$ mm, $\theta_1 = 7.13°$, $n_1 = 1.0$, and $n_2 = 1.435$ [31]. Using these values, we obtain $l_2 = 173$ mm $- 1.44 l_1$, which indicates that a motion of the LDA probe by 1.00 mm outside the fluid represents a motion of the laser crossing point by 1.44 mm inside the fluid. This correction was applied to all velocity measurements taken inside the jet.

The size of the measurement volume of a LDA setup is a matter of discussion [16,17,30], as it depends not only on the waist size of the laser beams in the crossing but also

on the number of fringes that are actually detected by the photomultiplier and on the size of the seeding particles. In cases where the sensitivity of the photomultiplier is unknown or difficult to access, the waist width of the lasers at the crossing is generally accepted as an overestimate of the width $d_x$ of the measurement volume. This is the case for the system used here: a one-dimensional Dantec LDA (backscattering diode laser). The beam waist at the crossing is given by

$$d_x = \frac{4L\lambda_1}{\pi E w}, \tag{6}$$

where $w$ is the beam waist before focusing, and $L$ and $E$ are the focal length and the expansion ratio of the optical system, respectively [32]. The length $d_y$ and the height $d_z$ of the measurement volume are given by

$$d_y = \frac{d_x}{\sin\theta_1}, \quad d_z = \frac{d_x}{\cos\theta_1}. \tag{7}$$

For the LDA setup used here, $L = 120$ mm and $E = 2$; consequently $d_x = 36\ \mu$m, $d_y = 300\ \mu$m, and $d_z = 36\ \mu$m.

The effect of seeding particles in the flow can be estimated from Stokes's law, which determines the limiting frequency for which the particles follow an oscillation with a deviation of up to 1% [33,34]. This is given by

$$f_{\text{Stokes}} < \frac{0.1\mu}{\rho_p R^2}, \tag{8}$$

where $\rho_p$ is the density and $R$ is the radius of the particles, and $\mu$ is the viscosity of the liquid. For the experiments presented here, Dantec 10-$\mu$m silver-coated hollow glass spheres were used as seeding particles, and their properties give $f_{\text{Stokes}} <$ 100 kHz, which indicates that their use is appropriate for the frequencies utilized in this work.

## III. SIMULATION DETAILS

### A. Numerical method

The numerical simulations used a finite-element method first developed for the study of creeping flow of dilute polymer solutions [35]. The method has since been extended to deal with inertial flows and used to model drop-on-demand printing of viscoelastic inks [36]. The finite-element mesh is Lagrangian in nature, i.e., the nodes advect with the fluid flow.

To model the experiments it was assumed that the only body force acting on the fluid was gravity, and that there were no significant temperature variations, so that the fluid density and viscosity were constant. The governing equations were therefore taken to be the Navier-Stokes equations. Drag due to air resistance was neglected in the simulations.

The velocity and pressure fields were discretized over a mesh of irregular triangular $P_1$-$P_1$ Galerkin elements; they were assigned values at each mesh node, and their values elsewhere were determined through linear interpolation. An artificial stabilization was employed in order to prevent spurious numerical pressure oscillations: the value of the stabilization parameter was optimized with respect to the spectral properties of the discrete coefficient matrix [35]. A $\theta$ scheme was used for the discrete time stepping, and the resulting difference equations were linearized via Picard iteration. Within each iteration, the linear system was solved numerically by the minimal residual (MINRES) method [37]. The size of the time step $\delta t$ was adaptively restricted by a Courant-Friedricks-Lewy condition of the form $U\delta t < \delta x$, where $U$ is a typical flow velocity and $\delta x$ is a typical element size. The position of each mesh node (except those on the printhead inlet boundary) was updated after each time step using the converged velocity solution for that node. The nodes on the printhead inlet present a special case: their positions were held constant in order to preserve the printhead shape and the applicability of the velocity modulation boundary condition (see Sec. III B).

To maintain element shape quality throughout the simulations, local mesh reconnections were made between time steps in regions where significant element distortion had occurred. The criteria for reconnection were based on the attainment of the Delaunay triangulation, which is optimal in two dimensions for a given set of node positions and can be efficiently obtained from any initial triangulation [38]. The local mesh resolution was also maintained by the addition of new nodes in depleted regions and the removal of nodes in congested regions.

In order to simulate the capillary breakup of the jet, the fluid domain was subdivided when the local jet radius fell below a certain threshold (here taken as <1% of the nozzle outlet radius). No method of coalescence was implemented in the simulations.

### B. Boundary conditions

The shape of the printhead used in the simulations was chosen to replicate the dimensions of the experimental nozzles, while simplifying the interior of the printhead apparatus above the nozzle. The initial finite-element grid with a nozzle of aspect ratio 1 is shown in Fig. 5. A slight fillet was applied to the sharp corner where the conical and straight nozzle sections meet. The top boundary of the grid is the printhead inlet,

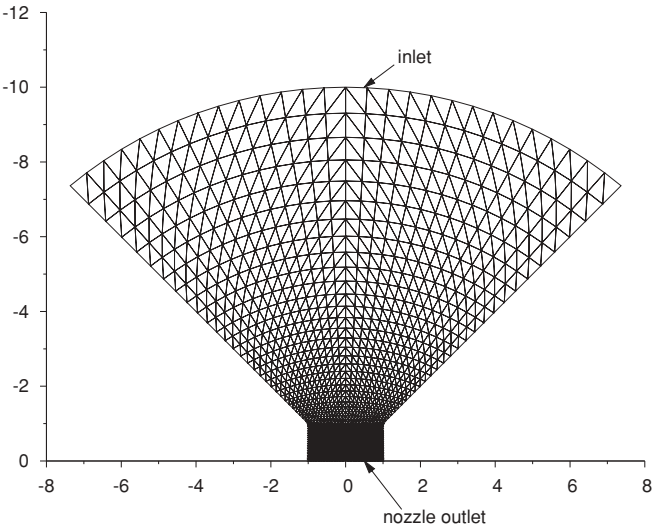


FIG. 5. The initial grid used in the simulations with a nozzle of aspect ratio 1. Similar grids with nozzles of aspect ratios 0 and 2 were also used. Axisymmetry was assumed, so that only half of the displayed domain was simulated. The unit of length was 1.1 mm (i.e., the nozzle radius in the experimental apparatus).

at which a time-dependent velocity boundary condition was imposed to represent the action of the membrane motion in the experiments (see below). The bottom boundary of the grid is the nozzle outlet: the coordinate origin was taken as the center of this outlet, and the initial shape of the fluid meniscus was flat (as in the experiments). The other boundaries of the grid are the rigid interior walls of the printhead and nozzle, at which boundary conditions of no slip were imposed. A standard surface tension boundary condition (see [36]) was applied at the meniscus and at fluid-air interfaces formed outside the printhead during the simulations. The contact line between the fluid and the interior walls of the nozzle was held pinned at the edge of the nozzle outlet. The fluid within the printhead was assumed to be initially at rest. Axisymmetry about the vertical jetting axis was assumed, although in the figures presented here we show reflected snapshots of the simulated jet for clarity in comparison with experimental photographs.

In order to drive the jetting in the simulations, a time-dependent velocity boundary condition was imposed uniformly over the printhead inlet surface in an inward normal direction. While this was not expected to fully represent the experimental flow throughout the entire printhead, it was designed to produce sufficiently similar flow conditions in the vicinity of the nozzle to yield a good correspondence between the simulated and experimental jets. For an unmodulated jet with mean velocity $U$ at the nozzle outlet, the magnitude of the velocity applied at the inlet was

$$u_0 = \pi R^2 U / A_{\text{in}}, \tag{9}$$

where $R$ is the nozzle outlet radius and $A_{\text{in}}$ is the surface area of the printhead inlet surface. To simulate a jet with modulation of frequency $f$ and relative amplitude $\varepsilon$, the inlet velocity was prescribed in terms of time $t$ as

$$u_{\text{in}}(t) = u_0 [1 + \varepsilon \sin(2\pi f t)]. \tag{10}$$

The possible presence of higher harmonics in the jet actuation was neglected in the simulations.

## IV. RESULTS

### A. LDA data analysis and breakup curves

Previous studies have determined the behavior of the breakup length of modulated jets, either in terms of the excitation voltage of the modulation driver (usually a piezoelectric element), or in terms of the initial perturbation amplitude by assuming a linear relationship between the perturbation and the driver amplitudes [12,18]. In contrast, this work focuses on the measurement of the internal dynamics of the jet to obtain a breakup curve in terms of the amplitude of the internal oscillatory velocity of the jet. Although LDA has been used in the past to determine the velocity field inside liquid jets, it has not yet been used to measure internal velocity oscillations in modulated jets [16]. The experimental setup described in Sec. II was used with a 74.7% solution of glycerol in water (properties as given previously) and the nozzle of aspect ratio 1 to produce stable jets for three different cases, with droplet speeds of 3.6, 4.0, and 4.3 $\text{ms}^{-1}$ (measured just below the unmodulated jet breakup point). These jets had corresponding Reynolds numbers of 135, 150, and 161, and Weber numbers of 274, 338, and 391, respectively [cf. Eq. (1)], which are within the regime of commercial CIJ applications. In order to maintain a common droplet separation distance of $\lambda = 4.9d$ (where $d = 2.2$ mm is the nozzle diameter), the three jets were modulated with driving signals of frequencies 330, 370, and 398 Hz, respectively. In each case, several different values of the modulation amplitude were considered.

A series of LDA measurements was conducted for each set of jetting conditions. Measurements were taken at the center of each jet at a fixed axial position ($14d = 30.8$ mm below the nozzle plane). The average fluid velocity at the measurement position was approximately 10% lower than the average droplet speed immediately below the breakup point, due to gravity. Two data sets with an average of 20 000 jet velocity readings each were obtained for every different modulation amplitude. The LDA system was set up to record data at intervals of 1 ms, although because the recording of each LDA measurement is a random process, the data produced were not equally spaced in time [34]. Reconstruction of the LDA data was necessary in order to permit the use of the fast Fourier transform (FFT) algorithm, which requires equally spaced data. Therefore each missing data point (approximately one per thousand) was defined simply by repeating the value of the preceding data point; this procedure has been used elsewhere and exhibits a precision of 5% in FFT analyses [34]. Once reconstructed, the LDA data were analyzed using the FFT algorithm to obtain the Fourier spectrum for each case, i.e., the distribution of velocity contributions versus frequency. An example of the FFT results is shown in Fig. 6. Subharmonics were not detected within the jetting conditions studied in this work. The presence of higher harmonics could not be established, as the data acquisition rate of the experiments restricted the frequency analysis to values below 500 Hz (the Nyquist criterion).

In addition to the LDA measurements of jet velocity, single-flash shadowgraph images of each jet were recorded in the neighborhood of its breakup point. These images provided the visualization of jet and droplet shapes, and enabled the direct measurement of the stable breakup length for each set of jetting and modulation conditions. Rather than requiring

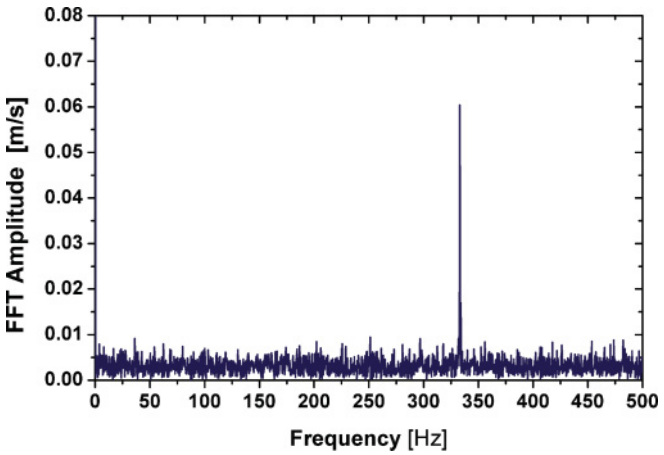


FIG. 6. (Color online) An example of the results of a fast Fourier transform analysis performed on reconstructed LDA data. The graph shows the Fourier spectrum of velocity measurements for a jet modulated by a 333-Hz sinusoidal perturbation.

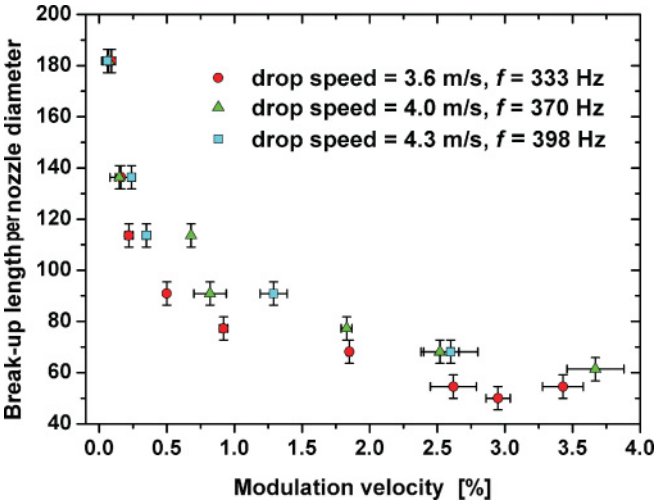


FIG. 7. (Color online) The breakup curves for three jets of different speeds, each modulated at a particular frequency chosen such that the droplet separation distances of all three jets were equal. The nozzle had a diameter of 2.2 mm and an aspect ratio of 1. LDA measurements were taken at the center of the jet 30.8 mm below the nozzle plane.

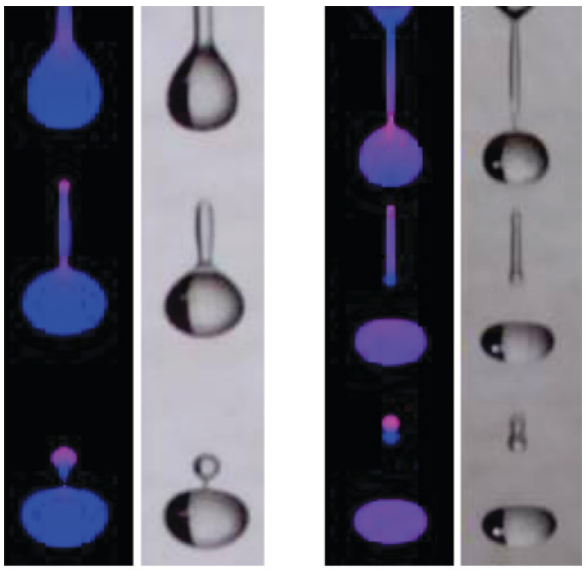


FIG. 8. (Color online) A comparison of the jet breakup shapes in the simulations (left) and the experiments (right) for two different modulation amplitudes (with other parameters equal). Cases (a) and (b) correspond to jets breaking up at distances of approximately 50$d$ and 82$d$ below the nozzle plane, respectively.

the very high resolution of other experimental setups, the present experiments required a large field of view to identify the position along the jet of the breakup point for the various conditions of modulation [28,39]. The breakup length of the modulated jet varied from 40 to 11 cm, a range imaged in a single frame by the camera system when positioned 5 cm below the nozzle plane. By combining the data obtained by the two separate measurement techniques, plots of the dimensionless breakup length versus velocity modulation amplitude were produced, as shown in Fig. 7. These plots are commonly referred to in industry as *breakup curves*. The $x$ coordinates of the data points on the breakup curves were derived from FFT analyses of the LDA results, and the $y$ coordinates from shadowgraph images. Horizontal error bars represent the difference between the two LDA data sets obtained for each experiment, while vertical error bars have been defined uniformly as the wavelength of the modulation, i.e., the approximate separation between droplets.

### B. Jet shapes

In Figs. 8 and 9 comparisons are shown of the jet shapes observed in the experiments (via shadowgraph imaging) and those computed by numerical simulations using the same jetting conditions. In Fig. 8 two jets (a) and (b) are shown, each corresponding to a different amplitude of modulation (with all other parameters equal). The images on the left-hand side in (a) and (b) are simulation snapshots, while those on the right-hand side are shadowgraph pictures. Each image has been cropped to show only the neighborhood of the jet breakup point. The droplet speed was 3.5 $\mathrm{m\,s^{-1}}$ (measured at the breakup point in the unmodulated case), and the modulation frequency was 333 Hz, giving a droplet separation distance $\lambda = 4.6d$; the Reynolds and Weber numbers were approximately 131 and 259. The nozzle of aspect ratio 1 was used for these comparisons. The jetting direction is vertically downward. In the simulation snapshots, the shading or coloring indicates the local vertical velocity component (lighter shades are moving faster).

In both cases, Figs. 8(a) and 8(b), there is a close similarity between the simulated and experimental jets; analogous agreement was found over a range of parameters. The slightly longer droplet tails visible in the simulation snapshot of case (a), compared to the corresponding shadowgraph picture, are due to a small relative time lag between the two images.

Figure 8 also illustrates the influence of the amplitude of the modulation on the breakup dynamics and droplet distribution of the jets. In (b), with a low modulation amplitude of approximately 1%, the jet shape was almost fore-aft symmetric between the main beads (which subsequently became the main droplets). Capillary pinchoff occurred almost simultaneously at both ends of the filaments between the beads, so that the detached filaments recoiled under surface tension to form smaller interspersed *satellite drops* traveling at almost the same speed as the main drops. Conversely, jet (a) had a greater amplitude of modulation of about 3%, causing enhanced nonlinear growth of the disturbance along the jet so that, far from the nozzle, the wave form was swept forward and the breakup was asymmetric as seen in the images. The pinchoff occurred at the rear of each filament, leaving each main droplet with a tail trailing behind it; these tails then retracted fully into the main bodies of the drops.

It is also worth noting that, in general, the first few droplets produced by a continuous jet are anomalous in size and shape with respect to subsequent drops, because of their dependence upon the initial condition of the flow prior to jetting (i.e., the shape and location of the meniscus at the nozzle). After the first few drops have broken away from the main jet, the influence

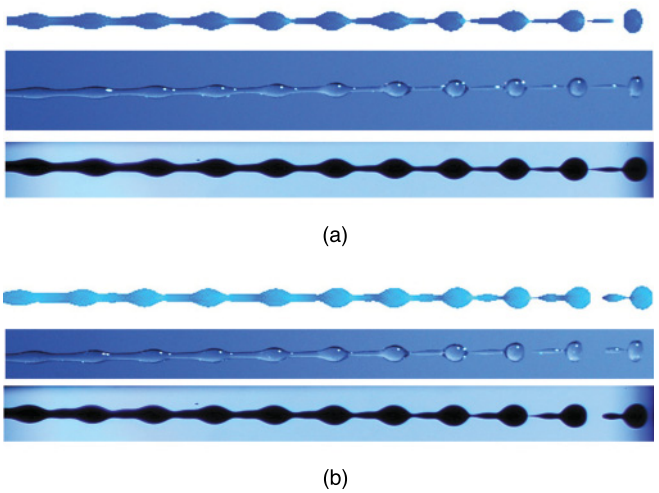


FIG. 9. (Color online) Comparisons of jet shapes for three models. In each case (a) and (b) the top image corresponds to the numerically simulated jet, the middle image corresponds to the large-scale experimental jet, and the bottom image corresponds to a real inkjet produced by a commercially available CIJ printer. Fluid and nozzle properties are such that Re $\approx$ 160 and We $\approx$ 400 for all three systems. The two cases (a) and (b) differ in the modulation amplitude; in case (a) the amplitude was 5% for the simulated and large-scale jets, while the electrical amplitude of the harmonic wave form in the commerical printhead was 55 V. In case (b) the corresponding values were 10% and 80 V.

of the precise initial condition is negligible, and the breakup characteristics of successive drops are practically identical.

Whereas Fig. 8 shows only the vicinity of the breakup points of simulated and large-scale jets, Fig. 9 shows longer sections of jets, consisting of about ten wavelengths behind the breakup point. Two cases (a) and (b) were considered, corresponding to two different modulation amplitudes of 5% and 10%, respectively (all other properties being equal); the Reynolds and Weber numbers were approximately 160 and 400, respectively (note that these differ from the cases in Fig. 8), and the jet breakup lengths were different in the two cases. The jetting direction was from left to right. For each case, Figs. 9(a) and 9(b), images of three jets are shown: the upper image is a simulation snapshot, the middle image is a shadowgraph picture of a large-scale jet produced by the generator described in Sec. II A, and the lower image was taken from a real industrial CIJ printer.

The development along the jet of the perturbation introduced by modulation at the nozzle can be seen in these images, which are qualitatively similar in each case. Case (a), having a relatively lower modulation amplitude, exhibits greater symmetry in the free-surface shape between consecutive peaks, although in the last few wavelengths the asymmetry becomes gradually more noticeable as the shape of the wave form increasingly leans forward with each subsequent wavelength due to its nonlinear evolution. In case (b), with a higher amplitude of modulation, the asymmetry of the perturbation is further exaggerated in its progression along the jet. This is particularly apparent in the last couple of wavelengths, where the connecting ligament between successive beads is considerably thicker at the front than at the back. Such breakup asymmetry is desirable industrially, due to the greater likelihood of the trailing tail retracting into the main body of each drop rather than breaking away to form a satellite drop.

The similarity of the three images shown in each case, Figs. 9(a) and 9(b), endorses both the Lagrangian simulations and the large-scale jet generator as representative of the jetting conditions in real inkjets. The bottom image shows a photograph of a real industrial inkjet, with nozzle diameter of order 50–100 $\mu$m, and although it is certainly possible to obtain well-resolved images of jets on this scale, it should be emphasized that it would be considerably more difficult to analyze the internal fluid velocity field using a technique such as LDA with sufficient accuracy.

### C. Velocity profiles

The effect of the nozzle geometry on the behavior of liquid jets is a topic of great interest to the inkjet community. Changes in the breakup length have been observed for jets produced by systems with different nozzle geometries [12] but the influence on the internal velocity field of jets has not been studied formally, either experimentally or numerically.

In a separate series of experiments, velocity profiles were measured within unmodulated jets in order to study the effects of the nozzle geometry on the velocity distribution below the nozzle. In these experiments three different nozzles of aspect ratios (AR) 0, 1, and 2 were tested; the dimensions of these nozzles are shown above in Fig. 3. The jetting conditions were adjusted to produce an average jet velocity of 3.6 ms$^{-1}$ at the furthest measuring point downstream, which was a distance of 110 mm below the nozzle plane (i.e., 50 nozzle diameters). Based on this velocity, the Reynolds and Weber numbers of these jets were 135 and 274, respectively. The velocity profiles were obtained from LDA measurements at six axial positions along the jet, which were at distances of 1, 3, 5, 7, 9, and 11 cm from the nozzle. At each axial position, readings were taken separately at 15 radial locations, evenly distributed across the jet. The choice of measurement positions was restricted physically by the dimensions of the actuator and the LDA probe, and by the separation and angle of the lasers. As a consequence, measurements could not be obtained at distances closer to the nozzle than 10 mm.

Some examples of the velocity profiles are plotted in Fig. 10. Profiles are shown at three axial positions along the jet; the nozzle of aspect ratio 2 was used in this case. The vertical (velocity) error bars are based on standard deviation analyses over approximately 20 000 LDA measurements near the jet axis, and approximately 8000 near the jet surface. Horizontal (position) error bars are not shown, but correspond to the length $d_y$ of the LDA measurement volume, i.e., $\pm$0.15 mm.

At 1 cm from the nozzle, the velocity profile retained a pipe-flow shape indicative of recent emergence from the relatively long nozzle, whereas further along the jet at 3 cm and particularly 11 cm from the nozzle, the profiles had become much flatter. At 3 cm enough profile structure was captured to observe that the jet was still definitely faster in the center than at its surface, with a mean velocity across the jet of roughly 3.4 ms$^{-1}$. At 11 cm only error-sized deviations from a straight line were recorded and no definitive profile variation could be

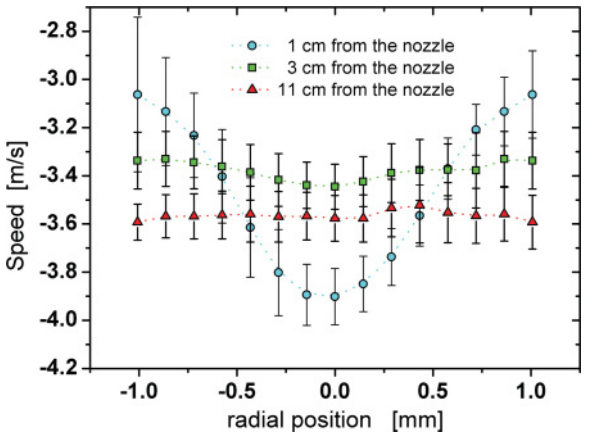


FIG. 10. (Color online) Three velocity profiles of a real unmodulated jet using the nozzle of aspect ratio 2. Each data point was derived by analyzing a set of LDA velocity measurements.

extracted; the mean velocity there was about 3.6 $ms^{-1}$, the increase being due to gravity.

Analogous velocity profiles were also calculated numerically via simulations of jets using the same flow conditions as in the experiments; those corresponding to the experimental jet profiles of Fig. 10 are shown in Fig. 11. Comparison of the two figures shows good quantitative agreement. It should be re-emphasized that jet axisymmetry was assumed in the numerical method, thus in Fig. 11 only the right-hand half of each profile was computed by the simulation, and the left-hand halves are mirror images.

An alternative illustration of the velocity variation throughout each jet is provided by the set of interpolated two-dimensional heat maps shown in Fig. 12. Each heat map corresponds to a different value of the nozzle aspect ratio, namely 0, 1, and 2 for the top, middle, and bottom maps, respectively. For each nozzle, velocity profiles were obtained for six axial positions and each profile was composed of velocity readings derived from LDA measurements at 15 different radial locations, therefore a total of 90 velocity data

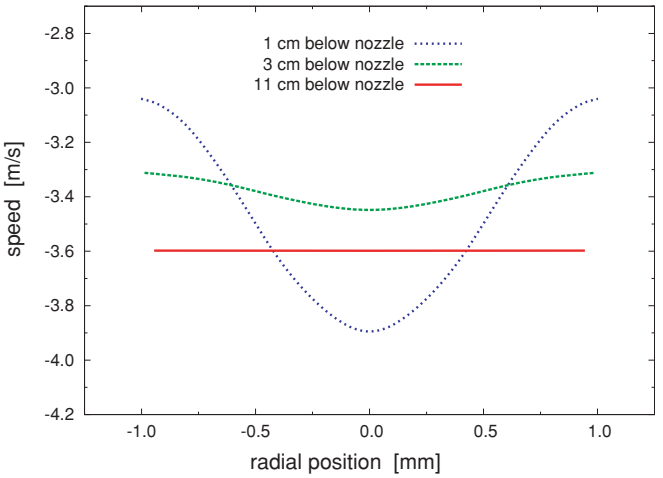


FIG. 11. (Color online) Three velocity profiles of a simulated unmodulated jet using the nozzle of aspect ratio 2. The simulation parameters were chosen to match the jetting conditions of the experiments.

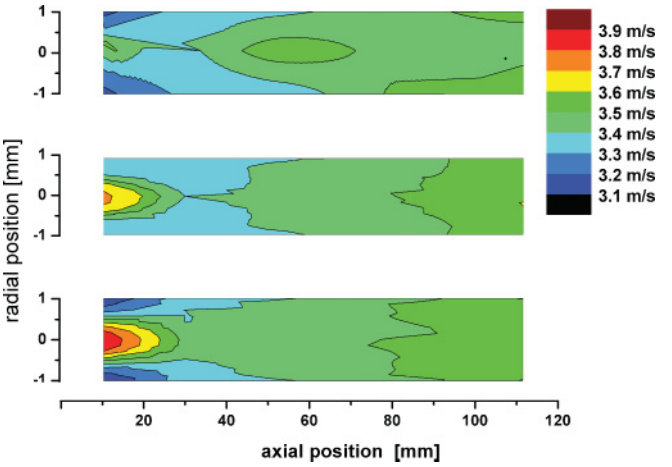


FIG. 12. (Color online) Velocity field heat maps of real unmodulated jets, obtained via LDA measurements for three different nozzles. The top, middle, and bottom heat maps correspond to nozzles with aspect ratios 0, 1, and 2, respectively.

points were used to create each of the three heat maps (each data point being the result of averaging approximately 8000 to 20 000 velocity readings).

As expected, the variation in the velocity field was found to increase with nozzle length, as the longer residence time of each fluid element in the cylindrical section of a longer nozzle enhances the pipe-flow shape of the local jet profile, and thus causes the persistence of this shape further along the jet than in the case of a shorter nozzle. The profiles of all three jets were virtually flat at distances of around 5 cm and above.

In Fig.13 the equivalent heat maps for the three simulated jets are shown. Again there is good correlation with the experimental results for all three jets over the full axial range under consideration. The simulated jets were axisymmetric by assumption of the method, so that only the top half of each heat map represents the computational domain, and the lower half is a reflection in the jet axis.

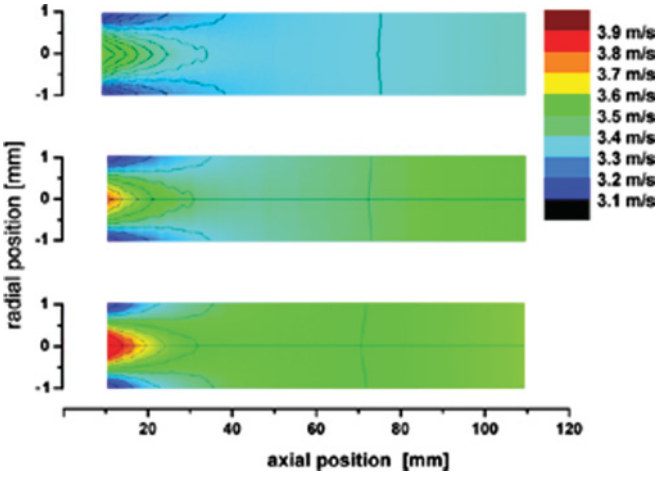


FIG. 13. (Color online) Velocity field heat maps of simulated unmodulated jets, for three different nozzle aspect ratios of 0, 1, and 2 (top, middle, and bottom maps, respectively). The nozzle dimensions and flow conditions emulate the experimental settings.

## V. CONCLUSIONS

This work presents a scheme whereby experimental and numerical simulations can be conducted under very similar conditions and where the dynamics of the flow of jets can be obtained and compared. Experiments and numerical simulations of modulated and unmodulated pressure-driven liquid jets have been presented. The experimental setup which is capable of producing millimeter-sized jets and permits the direct observation and measurement of the velocity field along the jet, and the jet shape and breakup dynamics, has been tested and its results reported. The application of laser Doppler anemometry to liquid jets to measure the velocity modulation amplitude in millimeter-size jets was presented. Laser Doppler anemometry was also used to obtain the velocity profiles of three liquid jets flowing from different nozzle geometries. Numerical results obtained using a Lagrangian finite-element method have been compared with the experimental data with good agreement, both qualitative and quantitative, demonstrating the ability of the simulations to accurately replicate continuous Newtonian jets. This validated numerical model may be used to explore critical scenarios such as the jetting of molten metals, the printing of hazardous chemicals, or to conduct further studies of fluid dynamical aspects. Current and future studies with the experimental setup and the numerical model include investigations of the jetting dynamics of viscoelastic fluids, the dynamics of liquid filaments, and the elimination of satellite droplets.

## ACKNOWLEDGMENTS

This project was supported by the UK Engineering and Physical Sciences Research Council, and by the industrial partners in the "Next-Generation Inkjet Technology" consortium. The authors are also grateful to M. R. Mackley for the loan of the LDA equipment.

[1] J. Eggers and E. Villermaux, Rep. Prog. Phys. **71**, 036601 (2008).
[2] J. W. Strutt (Lord Rayleigh), *The Theory of Sound* (Macmillan, London, 1894), Vol. II.
[3] H. Dong, W. W. Carr, and J. F. Morris, Rev. Sci. Instrum. **77**, 085101 (2006).
[4] J. Eggers, Rev. Mod. Phys. **69**, 865 (1997).
[5] O. A. Basaran, AIChE J. **48**, 1842 (2002).
[6] J. Eggers, Phys. Rev. Lett. **71**, 3458 (1993).
[7] A. Frohn and N. Roth, *Dynamics of Droplets* (Springer-Verlag, Berlin, 2000).
[8] H. Wijshoff, *IS&T—NIP22: International Conference on Digital Printing Technologies* (Society for Imaging Science and Technology, Virginia, 2006), pp. 79–82.
[9] E. P. Furlani and M. S. Hanchak, Int. J. Num. Meth. Fluids, doi:10.1002/fld.2205.
[10] C. A. Bruce, IBM J. Res. Dev. **20**, 258 (1976).
[11] D. P. Busker and A. P. G. G. Lamers, Fluid Dyn. Res. **5**, 159 (1989).
[12] B. Lopez, A. Soucemarianadin, and P. Attané, J. Imaging Sci. Technol. **43**, 145 (1999).
[13] I. M. Hutchings, G. D. Martin, and S. D. Hoath, J. Imaging Sci. Technol. **51**, 438 (2007).
[14] J. R. Castrejón-Pita, G. D. Martin, S. D. Hoath, and I. M. Hutchings, Rev. Sci. Instrum. **79**, 075108 (2008).
[15] S. A. Curry and H. Portig, IBM J. Res. Dev. **21**, 10 (1977).
[16] D. González-Mendizabal, C. Olivera-Fuentes, and J. M. Guzmán, Chem. Eng. Commun. **56**, 117 (1987).
[17] T. Battal, C. D. Bain, M. Weiss, and R. C. Darton, J. Colloid Interface Sci. **263**, 250 (2003).
[18] A. Kalaaji, B. Lopez, P. Attané, and A. Soucemarianadin, Phys. Fluids **15**, 2469 (2003).
[19] N. Vágó, Á. Spiegel, P. Couty, F. R. Wagner, and B. Richerzhagen, Exp. Fluids **35**, 303 (2003).
[20] A. Cervone, S. Manservisi, and R. Scardovelli, J. Comput. Phys. **229**, 6853 (2010).
[21] A. A. Dolinsky *et al.*, Russ. J. Eng. Thermophys. **17**, 130 (2008).
[22] J. Luo *et al.*, Trans. Nonferrous Met. Soc. China **18**, 686 (2008).
[23] J. M. Chwalek *et al.*, Phys. Fluids **14**, L37 (2002).
[24] C. D. Meinhart and H. Zhang, J. Microelectromech. Syst. **9**, 67 (2000).
[25] LDS Test and Measurement Ltd., *Installation and Operating Manual, V200 series, Manual 892071*, 2nd ed. (LDS, Royston, England, 1995).
[26] Entran Sensors & Electronics, *EPX Pressure Sensors, Miniature Threaded Stainless Steel Diaphragm Specification Sheet* (Entran Sensor and Electronics, Fairfield, NJ, ISSUE PB0, 2008).
[27] R. J. Donnelly and W. I. Glaberson, Proc. R. Soc. London, Ser. A **290**, 547 (1966).
[28] A. U. Chen and O. A. Basaran, Phys. Fluids **14**, L1 (2002).
[29] R. C. Weast, *Handbook of Chemistry and Physics*, 57th ed. (CRC, Cleveland, 1997).
[30] R. J. Adrian, in *Fluid Mechanics Measurements*, edited by R. J. Goldstein (Hemisphere, Washington, DC, 1983), pp. 155–244.
[31] M. P. I. V. Iyer and F. L. Usher, J. Chem. Soc., Trans. **127**, 841 (1925).
[32] Dantec, Product Information P1270003 (Tonsbakken, Denmark, 2003).
[33] L. E. Drain, *The Laser Doppler Technique* (Wiley, Chichester, 1980).
[34] J. R. Castrejón-Pita, A. A. Castrejón-Pita, G. Huelsz, and R. Tovar, Phys. Rev. E **73**, 036601 (2006).
[35] O. G. Harlen, J. M. Rallison, and P. Szabó, J. Non-Newtonian Fluid Mech. **60**, 81 (1995).
[36] N. F. Morrison and O. G. Harlen, Rheol. Acta **49**, 619 (2010).
[37] C. C. Paige and M. A. Saunders, SIAM J. Numer. Anal. **12**, 617 (1975).
[38] H. Edelsbrunner, Acta Numerica **9**, 133 (2000).
[39] A. U. Chen, P. K. Notz, and O. A. Basaran, Phys. Rev. Lett. **88**, 174501 (2002).